buildings

MDPI

Article

Experimental Study on the Influence of Sidewall Excavation Width and Rock Wall Slope on the Stability of the Surrounding Rock in Hanging Tunnels

Hao Zhang [1], Tianyu Luo [2], Zhao Xiang [1,3], Zhiwei Cai [1,*], Tongqing Wu [4,*], Dong Zhang [5], Bing Liu [2] and Hu Feng [6]

[1] CCTEG Chongqing Engineering (GROUP) Co., Ltd., Chongqing 400016, China
[2] School of Architecture and Luqiao, Chongqing Vocational College of Transportation, Chongqing 402260, China
[3] Guang'an Vocational & Technical College, Guang'an 638000, China
[4] School of Civil and Hydraulic Engineering, Chongqing University of Science and Technology, Chongqing 401331, China
[5] Qinyuan Technology Co., Ltd., Chengdu 610213, China
[6] Chongqing Mas Sci. & Tech. Co., Ltd., Chongqing 400052, China
* Correspondence: caizhiwei@cqmsy.com (Z.C.); wutongq@cqust.edu.cn (T.W.)

Abstract: Hanging tunnels are a unique type of highway constructed on hard cliffs and towering mountains, renowned for their steep and distinctive characteristics. Compared to traditional full tunnels or open excavations, hanging tunnels offer significant advantages in terms of cost and construction time. However, the engineering design and construction cases of such tunnels are rarely reported, and concerns about construction safety and surrounding rock stability have become focal points. Taking the Shibanhe hanging tunnel as a case study, this paper focuses on the stability of the surrounding rock during the excavation of limestone hanging tunnels using physical analog model (PAM) experiments and numerical calculation. Firstly, based on the similarity principle and orthogonal experiments, river sand, bentonite, gypsum and P.O42.5 ordinary Portland cement were selected as the raw materials to configure similar materials from limestone. Secondly, according to the characteristics of hanging tunnels, geological models were designed, and excavation experiments with three different sidewall excavation widths and rock wall slopes were carried out. The effects of these variables on the stress and displacement behavior of the surrounding rock were analyzed, and the laws of their influence on the stability of the surrounding rock were explored. Finally, numerical simulations were employed to simulate the tunnel excavation, and the results of the numerical simulations and PAM experiments were compared and analyzed to verify the reliability of the PAM experiment. The results showed that the vertical stress on the rock pillars was significantly affected by the sidewall excavation widths, with a maximum increase rate of 53.8%. The displacement of the sidewall opening top was greatly influenced by the sidewall excavation widths, while the displacement of the sidewalls was more influenced by the rock wall slope. The experimental results of the PAM are consistent with the displacement and stress trends observed in the numerical simulation results, verifying their reliability. These findings can provide valuable guidance and reference for the design and construction of hanging tunnels.

Keywords: hanging tunnel; physical analog model; tunnel excavation; rock wall slope; sidewall excavation width

Citation: Zhang, H.; Luo, T.; Xiang, Z.; Cai, Z.; Wu, T.; Zhang, D.; Liu, B.; Feng, H. Experimental Study on the Influence of Sidewall Excavation Width and Rock Wall Slope on the Stability of the Surrounding Rock in Hanging Tunnels. *Buildings* **2024**, *14*, 3477. https://doi.org/10.3390/buildings14113477

Academic Editors: Humberto Varum and Bingxiang Yuan

Received: 24 August 2024
Revised: 30 September 2024
Accepted: 21 October 2024
Published: 31 October 2024

1. Introduction

In recent years, China has undergone a period of accelerating highway, railway, and urban rail transit construction and development due to the implementation of the rural revitalization strategy, in particular in mountainous areas, which required building numerous tunnels. In 2022, China's rural highway mileage exceeded 4.53 million km

with prefectural, township, and village mileages of 0.699, 1.243 and 2.589 million km, respectively. By the end of 2022, China had built 24,850 highway tunnels, exhibiting a 6% increase compared with 2021 [1]. In remote areas in southwest China, highways are usually built near steep cliffs, which requires the additional construction of bridges, tunnels, or high slopes. In these cases, highway construction is complicated by the steepness and instability of slopes. In addition to high costs and severe environmental damage, large-scale tunnel excavation can trigger slope instability. Hanging tunnels offer a good solution to the above problems. As a special type of road, hanging tunnels are carved out in hard cliffs and high steep mountains.

Compared with conventional tunnels or open excavation, hanging tunnels are dug out by making openings in the sidewalls of the cliffs. This method solves various problems in tunnel construction, such as ventilation, illumination, and waste slag at the working face. In addition, favorable ventilation and illumination conditions are generally ensured in hanging tunnels, reducing energy consumption during tunnel operation. Hanging tunnels are aligned with the initial terrain and merge into the mountains, preventing large-scale sloping and mitigating damage to the surrounding environment. Furthermore, hanging tunnels fully leverage the stability of the rock masses and require no special protection or support, such as linings or local reinforcement, thereby involving much lower cost and less time [2,3]. In a sense, hanging tunnels have the dual attributes of tunnels and slopes. It can be imagined that the construction safety of a hanging tunnel is directly determined by the sidewall excavation width and rock wall slope. Therefore, it is necessary to study the influence of these two factors on the stability of the surrounding rock of the hanging tunnel.

According to incomplete statistics, there are currently more than 10 hanging tunnels in China, with a total length of about 30 km, most of which were spontaneously built by villagers from the 1990s to the early 21st century. Some hanging tunnels operate normally in China's mountainous areas where limestone is predominant, such as in the Guizhou, Henan, and Shanxi Provinces, see Figure 1c–f. Hanging tunnels have also been found in the United States, Pakistan, Greece, Saudi Arabia, and the Philippines, see Figure 1a,b. These hanging tunnels provide greater travel convenience for local residents and become famous tourist attractions to boost economic growth in mountainous areas. How to ensure the safe operation of a hanging tunnel, promote the construction of hanging tunnels under appropriate and necessary conditions, and choose the most reasonable and safe construction techniques with the highest economic efficiency in specific situations has become an urgent problem.

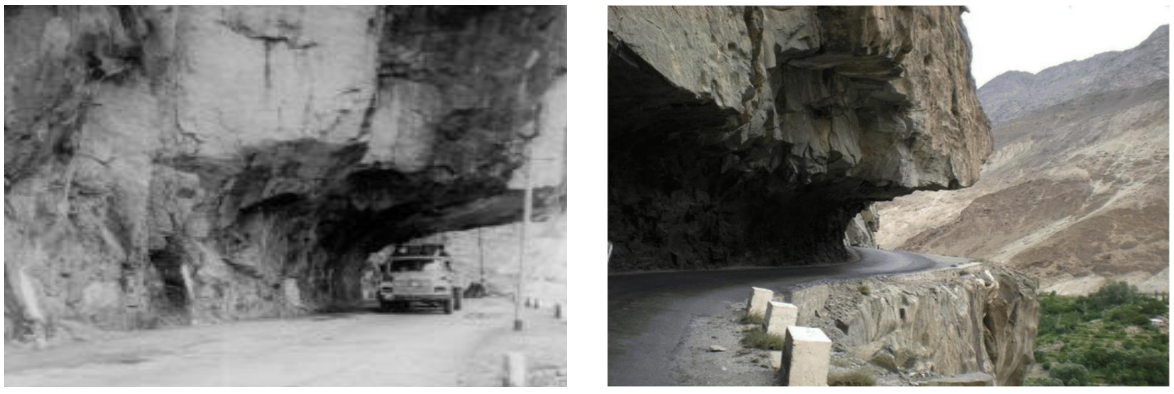

(**a**) (**b**)

Figure 1. *Cont.*

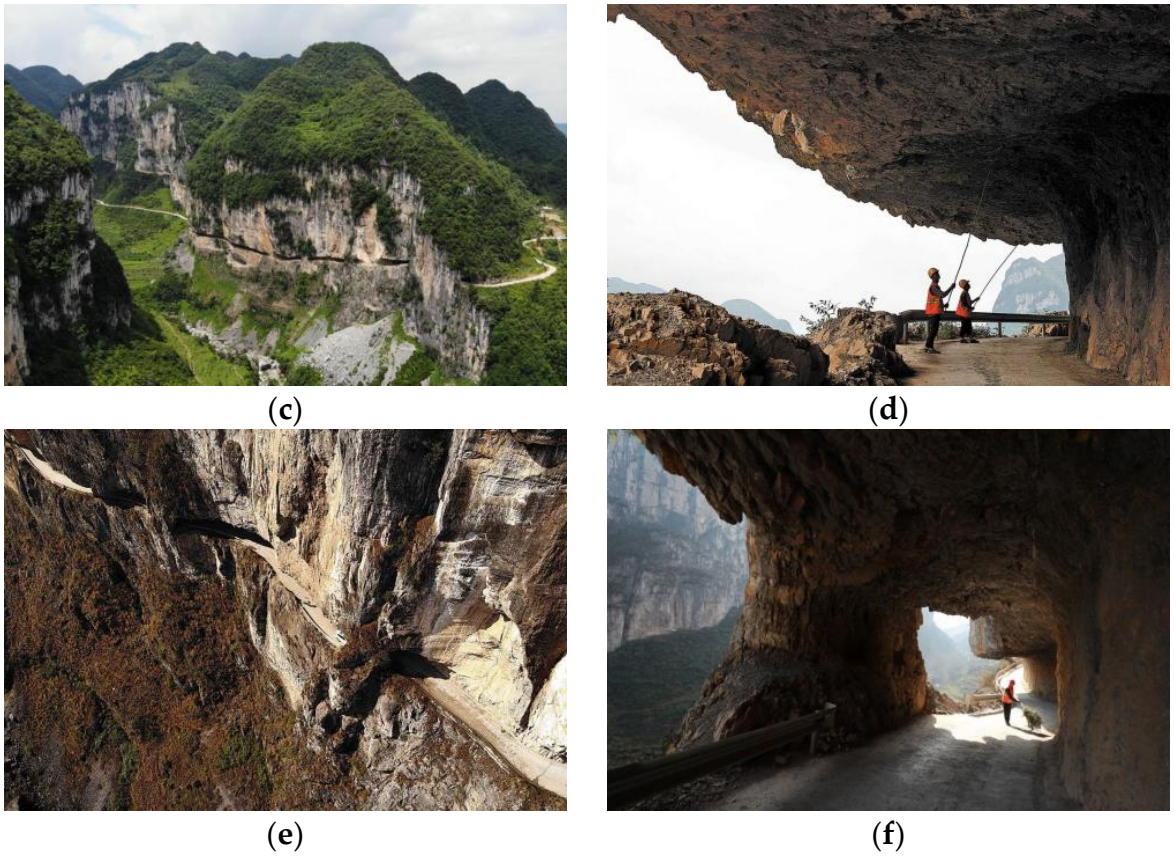

Figure 1. The hanging tunnels. (**a**) The half tunnel T-7 located in the Sutlej Valley of the western Himalayas, "Reprinted/adapted with permission from Ref. [2]. Copyright 2003, Anbalagan, R"; (**b**) the Ganji half tunnel located on Skardu Road near the Karakoram Highway, "Reprinted/adapted with permission from Ref. [3]. Copyright 2022, Emad, M."; (**c**–**f**) Shibanhe hanging tunnel in Guizhou Province, "Reprinted/adapted with permission from Refs. [4–6]. Copyright 2019, 2020, Xianpu Han".

In the case of hanging tunnels, the rock masses that undergo stress redistribution after excavation are considered in the surrounding rock, and their stability and safety form the foundation for the tunnel's engineering safety throughout its life cycle. The safety of the surrounding rock is an important indicator of underground engineering stability and depends on various factors, including rock mass strength, the geometric shape of the excavation, the stress induced around the tunnel entrance, construction methods, groundwater, and weathering processes [7]. The commonly used methods for stability analysis of the surrounding rocks in the tunnels include the following:

(1) Engineering analogy method [8–11]. The empirical approach, particularly the engineering analogy method, is the mainstream in surrounding rock and support structure design for tunnels. This method allows for the rapid formulation of preliminary support design schemes based on rock mass rating. However, it is impossible to obtain the stress and displacement distributions of surrounding rocks or perform a quantitative analysis of the mechanical performance of the surrounding rocks and support structures using this method.

(2) Theoretical analysis. Theoretical analysis centers on mechanical calculation, especially estimating surrounding rock stress. To be specific, the analytical approach is founded upon a series of empirical formulae derived from engineering practice [12–15] and those from mechanical theories [16,17]. These theoretical formulae are modified based on geological engineering conditions, rock mass conditions, excavation methods, and the characteristics of the tunnel itself [18–20]. The above references are all research results on the theoretical analysis of the stability of the rock surrounding the tunnel

under specific conditions. Considering that hanging tunnels have both tunnel and slope properties, it is difficult for us to directly apply them. However, the above references provide us with ideas and methods for the theoretical analysis of the stability of hanging tunnel-surrounding rock in the next step.

(3) Numerical simulation. The numerical approach usually yields intuitive results and involves the consideration of many influencing factors. Along with the rapid progress of computer technology, the finite element method [3,21–23], finite difference method [24–26], discrete element method [27–33], discontinuous deformation analysis method [34], and boundary element method [35] have been applied to predict surrounding rock stability. For example, Schlotfeldt et al. [36] and Tokashiki et al. [37] investigate the geotechnical aspects and stability of overhanging cliffs using numerical modeling. R. Anbalagan et al. [2] employed numerical analysis methods to investigate the distribution of stresses in the surrounding rock of half tunnels. Emad et al. [3] established a two-dimensional computational model of the Ganji half tunnel. They conducted a comparative analysis of the yielded volumes for tunnel heights ranging from 4.7 to 14.1 m while varying the tunnel span from 7 to 13 m, thereby exploring the stability of the surrounding rock of the half tunnel. This method only considers the effects of span size and tunnel height (i.e., the magnitude of the overlying load), and does not investigate the impact of different sidewall excavation widths and rock wall slope on the stability of the surrounding rock.

(4) Case analysis of field measurements. Various types of sensors are deployed in the construction areas to acquire data and observations, combined with the construction experience in other projects under similar conditions and the engineer's own experience to predict engineering safety [38–40]. To ensure the safety of tunnel construction, excavation methods or shield tunneling parameters can be adjusted based on the field-monitoring data. Although field tests can capture the deformation of surrounding rock and actual stress changes, installing the necessary testing components for a hanging tunnel connecting rural areas can be quite costly.

(5) Physical analog model (PAM) tests. It is still difficult to obtain field test measurements directly when performing a stability analysis for confining pressure in tunnels due to the complexity of the tunnel engineering itself. For this reason, numerical simulations are usually conducted instead. The numerical simulation has the advantages of clarified working principles, ease of use, and strong applicability. However, given the complexity of the tunnel-surrounding rocks, some mechanisms of mechanical response are as yet unclear, restricting the applicability of numerical simulation techniques. PAM tests can offer a full picture of the stress and deformation damage mechanisms, failure morphology, and instability phase under the joint action of engineering structures and rock and soil masses involved. PAM tests provide a convenient pathway to grasp mechanical properties, deformation and failure characteristics, as well as the stability of the surrounding rocks in the tunnels. Properly selecting analog materials and designing tunnel model test systems are vital for successful PAM tests. Analog materials are usually selected according to the similarity principle. For example, sand, quartz sand, and barite powder are used as aggregate [41–43], while cement, clay, and gypsum are used as cementing materials [44–46]. Various combinations of analog materials for tunnel-surrounding rocks are assessed via the orthogonal design. Next, a laboratory model test is conducted to thoroughly investigate various aspects and parameters of the tunnel, including the buried depth, weak intercalated layer, rupture failure mechanism, span, excavation method, and cross-sectional shape [47–50].

Wedge theory and numerical simulation are the mainstream methods of studying hanging tunnel stability. To clarify the effects of the opening width in the sidewalls and rock wall slope on the surrounding rock stability of a hanging tunnel, this study constructed a 1:20 scale indoor test PAM simulating the particular hanging tunnel in Shibanhe Village in Hezhang County of the Guizhou Province of China. PAM tests were conducted for different combinations of three sidewall excavation widths and three rock wall slopes, which

affect the hanging tunnel stress and displacement variations, as well as the surrounding rock stability. These were experimentally estimated, providing a deeper insight into the surrounding rock stability assessment in similar tunnel engineering scenarios.

2. Engineering Background

The Hanging Highway Tunnel in Shibanhe Village, Hezhang County, Guizhou Province of China, was taken as a case study. As shown in Figure 1d–f, this hanging tunnel is located in the northern part of the Yangtze/Pre-Yangtze Platform, with parallel fold bundles as the main structure, trending NE–SW. The folds are mostly elongated in shape, with the dip angle mainly gentle to moderate. The site has a middle mountain topography, with large elevation differences ranging from 1700 to 2100 m. The area has strong tectonic and erosion effects, with river valleys mostly in canyon form and the valley slopes mainly steep cliffs. Bedrock is exposed on the cliffs, with well-developed vegetation at the top and debris accumulation at the foot of the slope. The rock types in the area are mainly Permian Maokou Formation limestone, mainly light gray dolomite limestone, dolomite limestone, and marl, with some distribution of dolomite. The rock layers are mainly thick to very thick, with intact rock mass, no developed fractures, no groundwater, high rock strength, no support measures, and good slope and tunnel rock mass self-stability.

3. Methods

3.1. Similarity Principle

3.1.1. Basic Principles of Similarity Principle

Similarity principle provides a theoretical basis for physical analog model (PAM) design and testing. Its core idea is to establish a similarity relationship between the PAM and prototype via various similarity criteria concerning their geometry, dimensions, physical quantities, etc., so that the PAM test would reflect the objective laws of the prototype. The ratio of the same dimensional physical quantities in the prototype (P) and the model (M) is called the similarity scale, denoted by C. Geometric similarity is a prerequisite for other phenomena to be similar, and based on geometric similarity, other physical quantities can be derived through dimensional analysis, combined with geometric equations, physical equations, boundary conditions, etc.

According to the physics equation, the similarity relationship between displacement (C_δ), geometry (C_L), and strain (C_ε) similarity coefficients is as follows [44,46,50]:

$$C_\delta = C_L C_\varepsilon \tag{1}$$

Based on geometric and physical equations, as well as stress and displacement boundary conditions, the following similarity relationships can be derived [47,48]:

$$C_\sigma = C_\gamma C_L \tag{2}$$

$$C_\sigma = C_\varepsilon C_E \tag{3}$$

where C_σ and C_γ are stress and bulk density similarity coefficients, respectively.

According to dimensional analysis, if the similar scales of physical quantities with the same dimensions are equal, then the similarity ratio of dimensionless physical quantities is 1.

3.1.2. Determine the Similarity Coefficient

Hereinafter, the following designations are used: L is length, ρ is density, u is displacement, E is elastic modulus, σ is stress, σ_c is compressive strength, σ_t is tensile strength, ε is strain, f is internal friction coefficient, c is cohesive force, φ is internal friction angle, μ is Poisson's ratio, and k is permeability coefficient.

The respective similarity coefficients are as follows: C_μ is the Poisson's ratio similarity scale, C_ε is the strain similarity scale, C_f is the friction coefficient similarity scale, C_c is the cohesion similarity scale, C_φ is the internal friction angle similarity scale, C_σ is the stress

similarity scale, $C_{\sigma c}$ is the compressive strength similarity scale, $C_{\sigma t}$ is the tensile strength similarity scale, C_E is the elastic modulus similarity scale, C_L is the geometric similarity scale, and C_ρ is the density similarity scale.

According to similarity theory and the actual engineering background, the related design principles of the model hanging tunnels are presented in Table 1. In this test, based on the geometric dimensions of the prototype tunnel, as shown in Figure 3, and taking into account experimental conditions, testing costs, etc., the geometry ratio was determined to be $C_L = 20$. The other ratios can be obtained by solving Equations (1)–(3), and the results are shown in Table 1 [41,46,50].

Table 1. Similarity coefficients of key physical quantities of physical analog model (PAM) materials.

Key Physical Quantities	Dimension	Similarity Relation	Similarity Coefficient (Control Amount *)
Density (ρ)	ML^{-3}	C_ρ	1 *
Elastic modulus (E)	$ML^{-1}T^{-2}$	C_E	20 *
Poisson's ratio (μ)	Dimensionless	C_μ	1
Cohesion (c)	$ML^{-1}T^{-2}$	$C_c = C_E C_\varepsilon$	20
Internal friction angle (φ)	Dimensionless	C_φ	1
Stress (σ)	$ML^{-1}T^{-2}$	$C_\sigma = C_E C_\varepsilon$	20 *
Strain (ε)	Dimensionless	$C_\varepsilon = C_\rho C_g C_L {C_E}^{-1}$	1
Displacement (u)	L	C_L	20 *

Note: Parameters with "*" represent the key control quantity in each physical parameter, which strongly affect other parameters.

3.2. Similar Materials of PAM

3.2.1. Selection of PAM Materials

The similarity of model materials is an important prerequisite to ensure the accuracy of physical simulation results, and it significantly impacts the physical and mechanical properties of similar models. It is unrealistic to expect all physical quantities of similar materials to remain highly similar to the prototype. This article mainly studies the stress and displacement field changes of the surrounding rock in hanging tunnels under different widths of sidewall openings and slopes of rock walls. Therefore, it is only necessary to control the similarity of the main physical indicators of similar materials. Based on a large number of research results [41–46] and combined with engineering practice, orthogonal experiments were conducted to determine the optimal mix ratio using fine river sand as aggregate, gypsum powder, bentonite, and P.O42.5 ordinary Portland cement as binders. The raw materials are shown in Figure 2a.

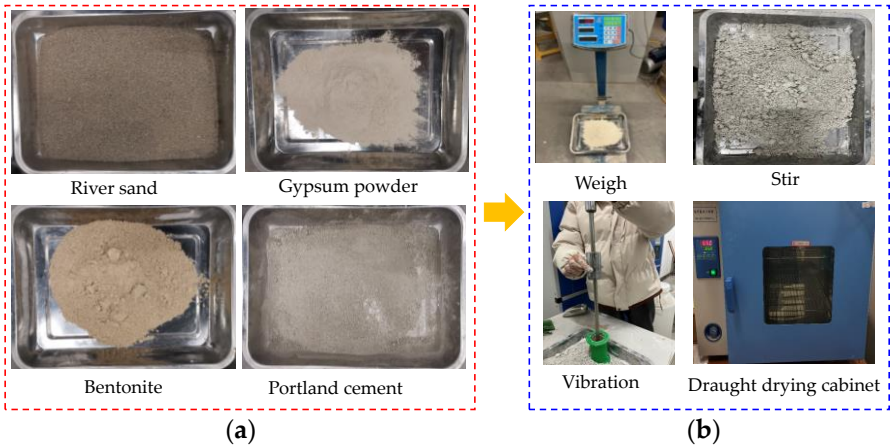

Figure 2. Raw materials and specimen preparation process. (**a**) The raw materials of surrounding rock; (**b**) steps in specimen preparation and maintenance.

3.2.2. Preparation of Samples

PAM materials were mixed with a water-to-cement ratio of 1:7 and a sand-to-cement ratio of 3:1; mix ratios of bentonite, gypsum powder, and cement in the binding materials were 2:7:1, 3:6:1, 4:5:1, 4:4:2, 5:3:2, and 5:4:1, respectively. Comprehensive PAM tests were conducted on samples with the above ratios. The raw materials and preparation steps of the specimens are as shown in Figure 2.

3.2.3. Testing of Basic Mechanical Parameters

Physical and mechanical parameters of the prepared PAM samples were determined via orthogonal tests, as shown in Table 2. Similarity coefficients obtained for various mix ratios are listed in Table 3. The model-to-prototype similarity degrees of groups with various mix ratios are summarized in Table 4. According to field investigation and laboratory mechanics experiment, the physical and mechanical parameters of the surrounding rocks are shown in Table 5. The similarity coefficients of elastic modulus, cohesion, and compressive strength are close to 20, and the similarity coefficients of weight, Poisson's ratio, and internal friction angle are close to 1. Therefore, the mix ratio of 451 sets between bentonite, gypsum powder, and ordinary Portland cement was selected as the optimal mix ratio.

Table 2. Physical and mechanical parameters of sample groups with various mix ratios.

Group	ρ/g/cm^3	σ_t/kPa	σ_c/kPa	μ	E/MPa	c/kPa	φ/°
271	1.96	185	1750	0.16	345	121.3	29
361	1.96	135	1417	0.16	294	125.4	32
451	1.93	126	1240	0.17	230	123.8	31
442	1.96	120	1182	0.17	195	121.8	33
532	1.93	119	1176	0.18	170	122.6	27
541	1.96	95	1257	0.17	152	124.6	32

Table 3. Similarity coefficients of sample groups with various mix ratios.

Group	C_γ	$C_{\sigma t}$	$C_{\sigma c}$	C_μ	C_E	C_c	C_φ
271	1.20	13.78	14.29	1.56	14.49	5.36	1.03
361	1.20	18.89	17.64	1.56	17.01	5.18	0.94
451	1.19	20.24	20.16	1.47	21.74	5.25	0.97
442	1.20	21.25	21.15	1.47	25.64	5.34	0.91
532	1.22	21.43	21.26	1.39	29.41	5.30	1.11
541	1.20	26.84	19.89	1.47	32.89	5.22	0.94

Table 4. Model-to-prototype similarity of each group.

Group	271	361	451	442	532	541
$C_\sigma/(C_L C_\gamma)$	0.60	0.74	0.85	0.88	0.87	0.83
C_E/C_σ	1.01	0.96	1.08	1.21	1.38	1.65

Table 5. Physical and mechanical parameters of the surrounding rocks.

Type	Young's Modulus E/MPa	Bulk Density γ/kN/m^3	Poisson's Ratio μ	Internal Friction Angle φ/°	Cohesion Force c/kPa	Compressive Strength σ_c/kPa	Tensile Strength σ_t/kPa
Model	230	19.26	0.17	31	123.8	1240	126
Prototype	5000	23.5	0.25	30	650	25,000	2550

3.3. Design and Testing of the Hanging Tunnel

3.3.1. Model Test Platform

The hanging tunnel under study mainly comprised low-grade mountain roads, with lower road grades and mostly two-way two-lane roads. Taking the actual situation of the Shibanhe hanging tunnel as the background, referring to the "Specifications for Design of Highway Tunnels Section 1 Civil Engineering" (JTG 3370.1-2018) [15], the hanging tunnel was designed as a circular arch structure with a radius of 4.4 m. The tunnel is 6.55 m high and 8.8 m wide, as shown in Figure 3a. The size of the sidewall openings was derived based on numerous engineering precedents with mostly irregular rectangular shapes, with a height of 55 cm below the tunnel vault, as shown in Figure 3b. The effect of the width of sidewall openings on the stability of the surrounding rock was analyzed; therefore, the height remains unchanged, while three widths of 500, 1000, and 4000 cm were used, as shown in Figure 3b. The tunnel section and the size of the sidewall openings are shown in Figure 3.

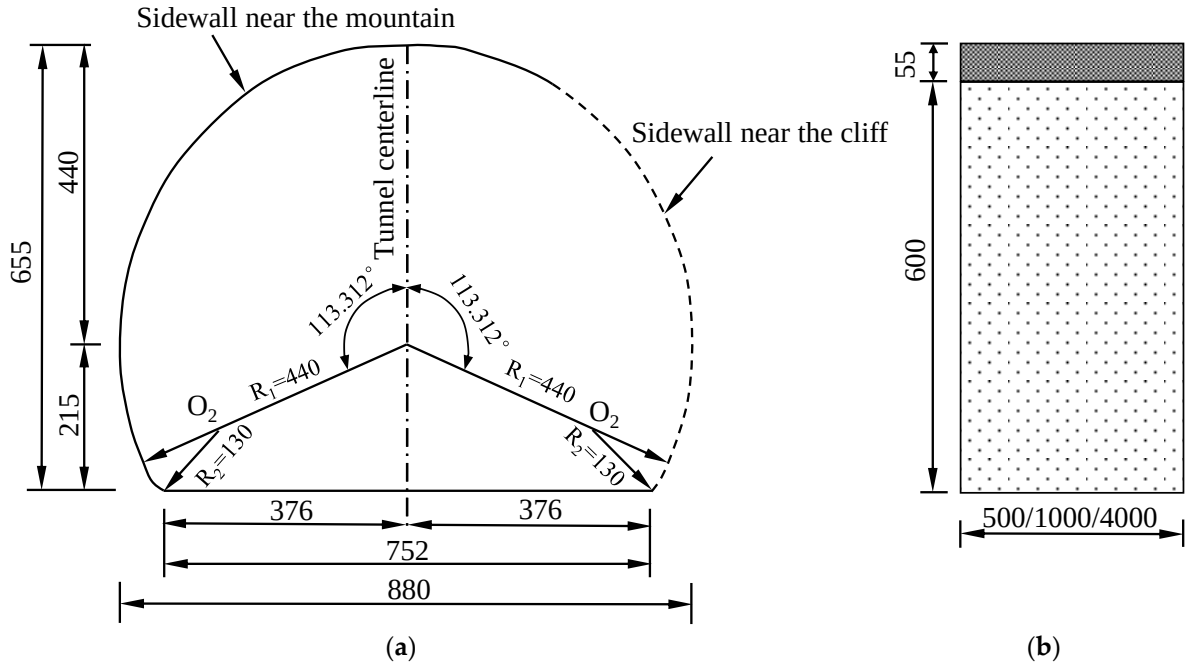

Figure 3. Tunnel cross-section and sidewall opening dimensions of the prototype hanging tunnel (unit: cm). (**a**) The sectional dimensions of the prototype hanging tunnel; (**b**) the dimensions of the sidewall openings.

Based on the geometric dimensions of the prototype tunnel, and taking into account experimental conditions, testing costs, etc., the geometric similarity ratio of the selected model was 1:20. Considering the tunnel's maximum burial depth, excavation width, length, etc., the height, width, and thickness of the PAM box were as follows: 2 m × 2 m × 2 m. Its main frame was welded from square steel, and 4 mm thick steel plates were used to enclosure the four sides. The entire model box was subdivided into faces 1–5, with face 1 and face 3 facing each other, where face 1 was movable to simulate differently inclined overburden faces in the test; face 2 and face 4 were opposite, representing tunnel excavation faces, as shown in Figure 4.

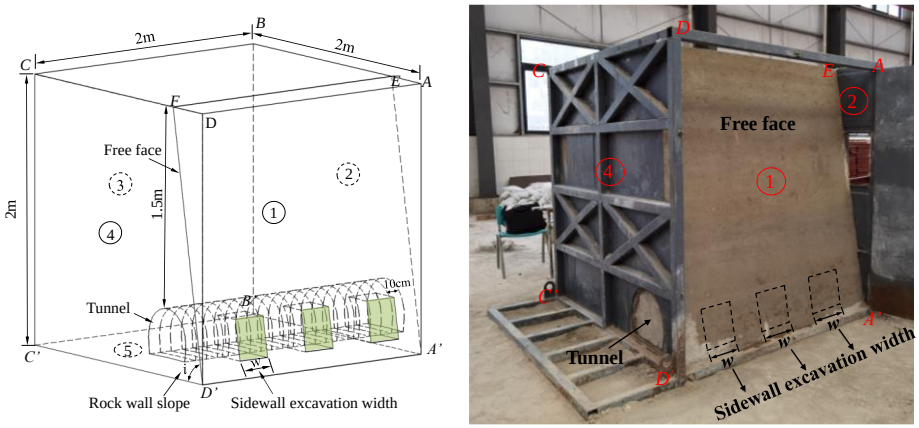

(**a**) (**b**)

Figure 4. Model test platform. (**a**) Schematic diagram of hanging tunnel model; (**b**) the PAM of hanging tunnel.

3.3.2. PAM Test Monitoring Scheme

The main purpose of this experiment was to monitor variations in internal rock stresses and displacements during the excavation process. In PAM experiments, the stability of tunnel-surrounding rock was analyzed by obtaining the stress and displacement of the surrounding rock. By burying soil pressure gauges, the stress changes in the surrounding rock at the monitoring points could be obtained, and by burying displacement sensors, the displacement changes in the monitoring points during excavation could be obtained. The measurement system included a miniature DMTY soil pressure gauge (diameter of 10 mm, thickness of 10 mm, and range of 0–100 kPa), a DMTY-type full-bridge embedded single-point displacement meter (with a 0.003 mm accuracy), and a DM-YB1820 dynamic and static strain measurement system (Nanjing Danmo Electronic Technology Co., Ltd., Nanjing, China), as shown in Figure 5.

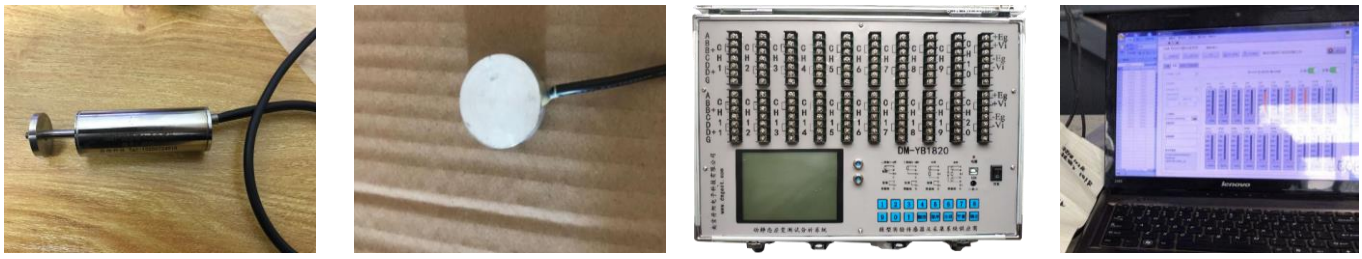

Micro displacement sensors | Micro soil pressure gauges | DM-YB1820 static strain gauge | Data acquisition system

Figure 5. PAM test measuring equipment.

In this study, one stress monitoring section was set at the rock pillar near the longitudinal middle of the tunnel; five soil pressure gauges were set at the tunnel sidewall near the mountain (1), the tunnel vault (2), the tunnel sidewall near the cliff (3), the tunnel floor (4) and the rock pillar (5). The soil pressure gauge on the side wall was vertically arranged to obtain its radial stress value, while other positions were horizontally arranged, as shown in Figure 6a. One displacement monitoring section was set along the longitudinal middle of the tunnel; four displacement meters were set at the tunnel sidewall near the mountain (1), the tunnel hance near the mountain (2), the tunnel vault (3) and the tunnel sidewall opening top (4), to collect radial displacement, as shown in Figure 6c. Layout diagram of measuring test components is shown in Figure 6.

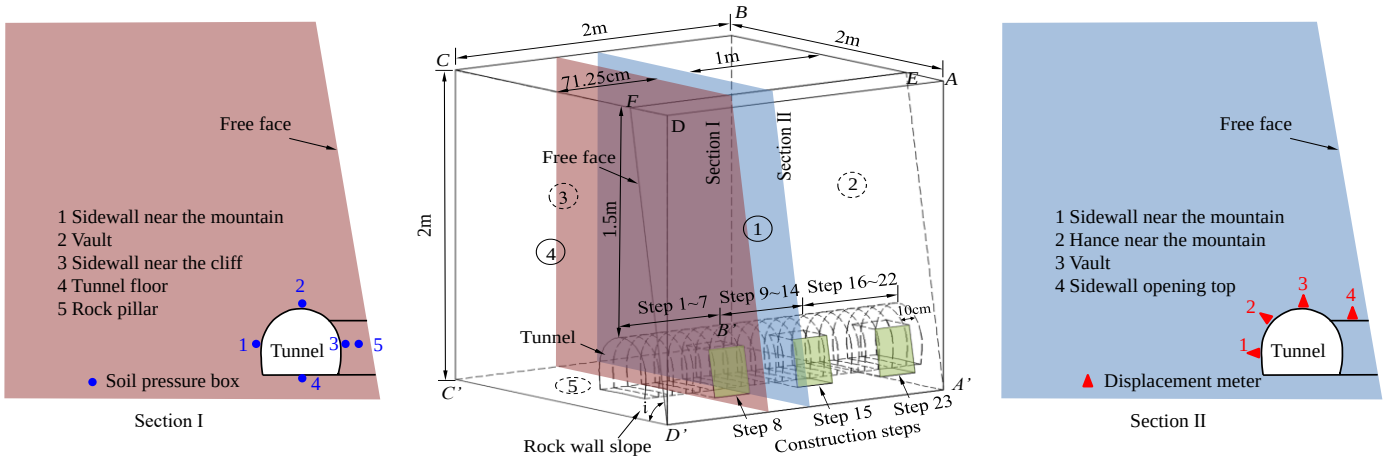

Figure 6. Layout diagram of measuring test components. (**a**) Schematic diagram of stress monitoring layout section; (**b**) schematic diagram of monitoring layout section; (**c**) schematic diagram of displacement monitoring layout section.

3.3.3. PAM Test Program

As already mentioned, the geometric scale of this indoor large-scale physical model test was 1:20. Based on the actual engineering situation and considering the cost issue of model tests, the working conditions of the model tests were simplified. Three sidewall widths and three rock wall slopes were used to provide nine working conditions for the tunnel-surrounding rock-stability-model test. The study investigated the effects of different rock wall slopes and sidewall excavation widths on the stability of hanging tunnel-surrounding rock. The test conditions are presented in Table 6.

Table 6. Test conditions.

Working Condition	1	2	3	4	5	6	7	8	9
Rock wall slope/°		80			85			90	
Sidewall excavation width/cm	25	50	200	25	50	200	25	50	200

3.3.4. PAM Elaboration Steps

Using the optimal mix ratio in the PAM test, the calculated amounts of filling materials were evenly mixed via a vertical mixer. Since the excavation process and surface of PAM did not reflect those of the actual hanging tunnel, 10 cm thick tunnel blocks made of steel plates were prefabricated according to the excavation tunnel profile via the layered filling method. To ensure smoothness and compaction of each layer, a 5 cm layer was filled each time, first leveled with wooden boards, then compacted with a self-made compactor. After filling to the tunnel position, the prefabricated tunnel blocks were placed in the predetermined position, filled as tightly as possible. After filling at the specified position, sensors were inserted/buried, recording the instrument number and position for later data collection. After filling was completed, the PAM top and open face were covered with plastic films for curing, and excavation was carried out one week later. This process is illustrated in Figure 7.

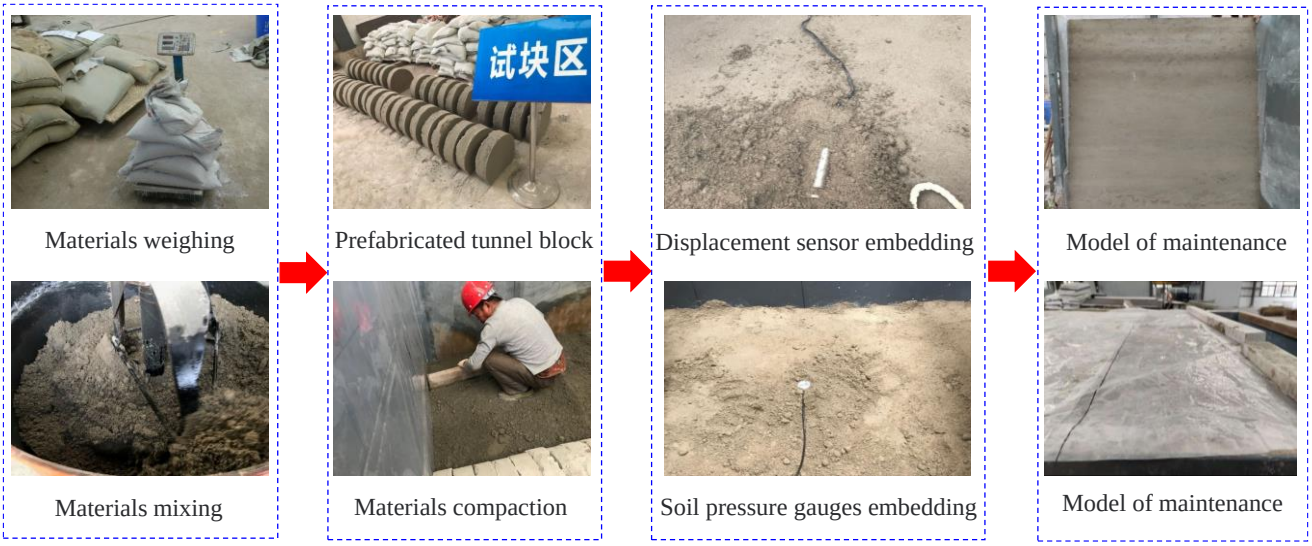

Figure 7. PAM elaboration scheme.

3.3.5. Model Test Steps

The PAM longitudinal length was 2 m, simulating full-section excavation tunneling. Each excavation (i.e., prefabricated tunnel block thickness) was 10 cm at a time. When reaching the sidewall opening, its excavation was carried out and repeated until completion of the hanging tunnel excavation process. After excavation, no support was provided in the physical model. Micro soil pressure gauges and displacement meters embedded in the model were used for stress and displacement monitoring, respectively. Before excavation, the sensor connector was wired to the stress–strain data acquisition instrument to collect the initial values. Data collection was immediately carried out after each excavation step to monitor variations in the surrounding rock stresses and strains during the excavation process. The PAM test steps and excavation process are depicted in Figure 8.

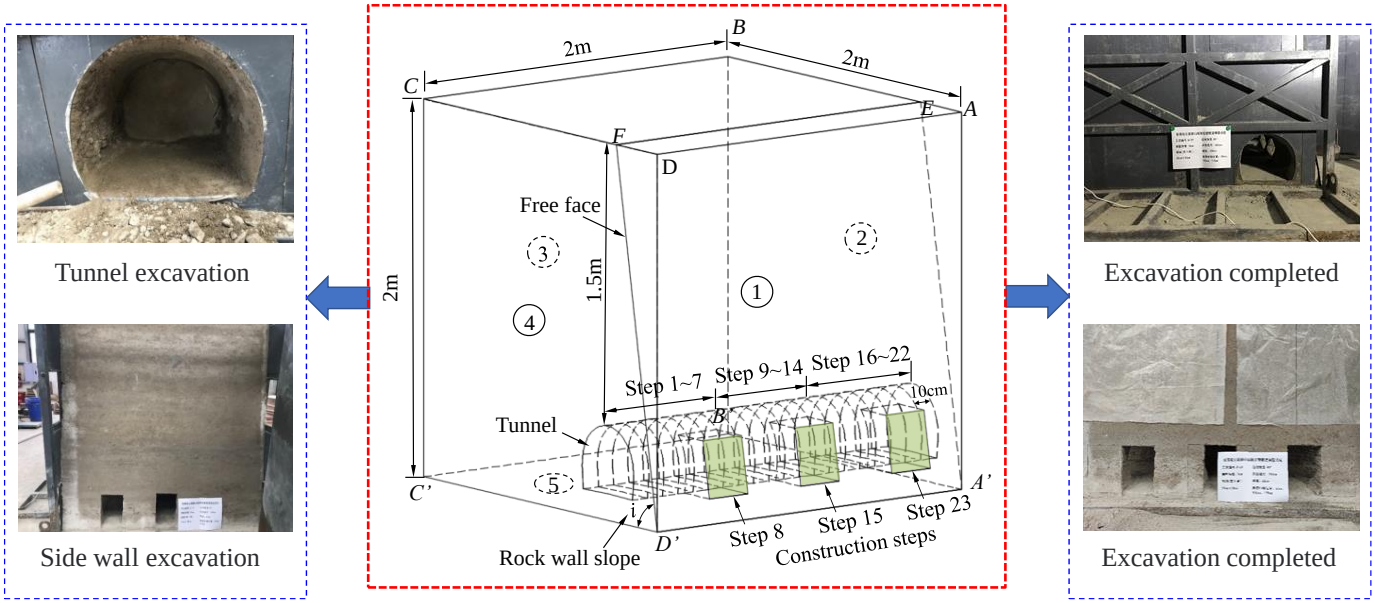

Figure 8. PAM test steps and excavation process.

4. Experimental Results and Analysis

4.1. Surrounding Rock Stress Distribution

4.1.1. Tests with Varying Sidewall Excavation Widths

The experimental assessment of the surrounding rock pressure used relative pressure values, i.e., pressure fluctuations after tunnel excavation, with positive values indicating a decrease in pressure and negative values indicating an increase in pressure. Figure 9 shows the excavation of different sidewall widths (25, 50, and 200 cm) under a rock wall slope of 80°, the stress curves of the sidewalls near the mountain, vaults, tunnel floors, sidewalls near the cliff, and rock pillars of the hanging tunnel model.

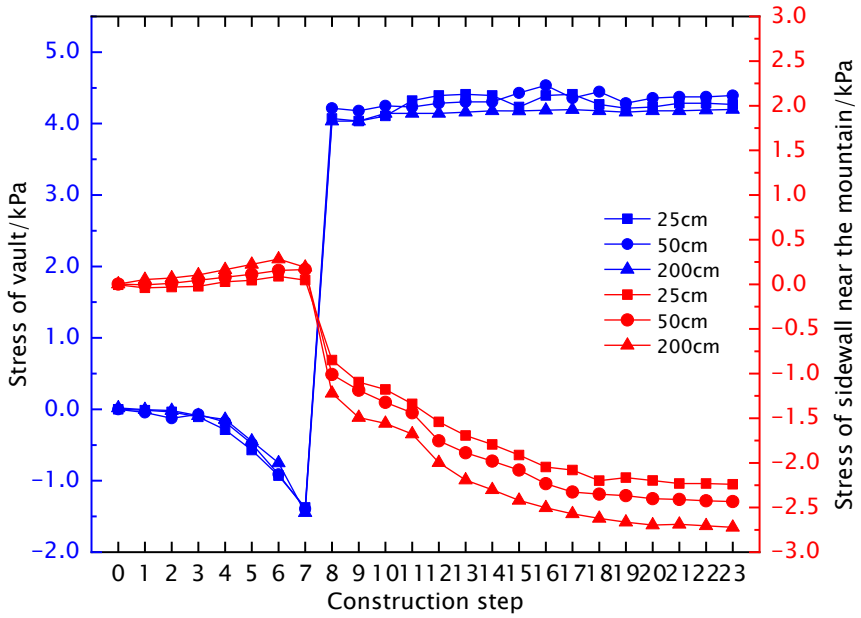

(**a**)

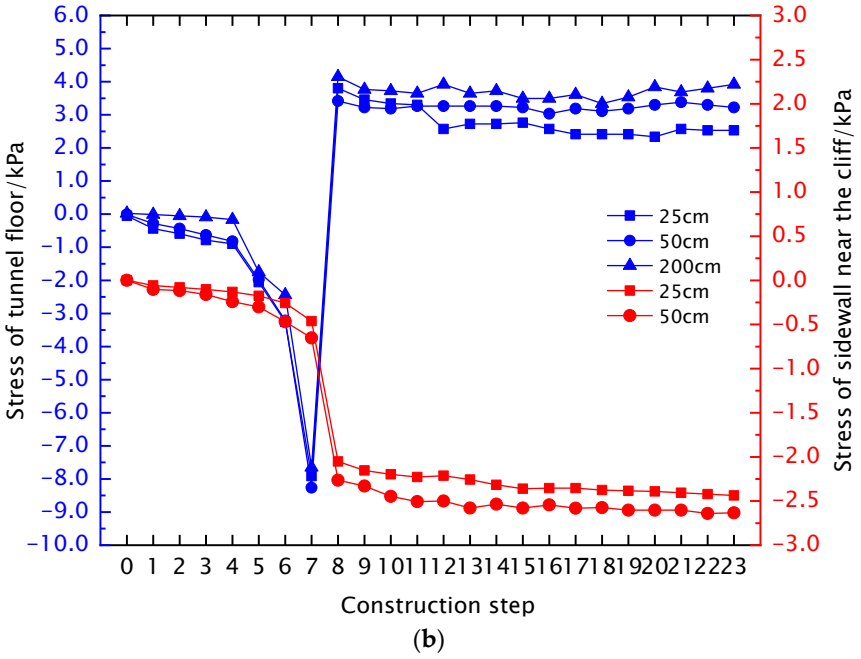

(**b**)

Figure 9. *Cont.*

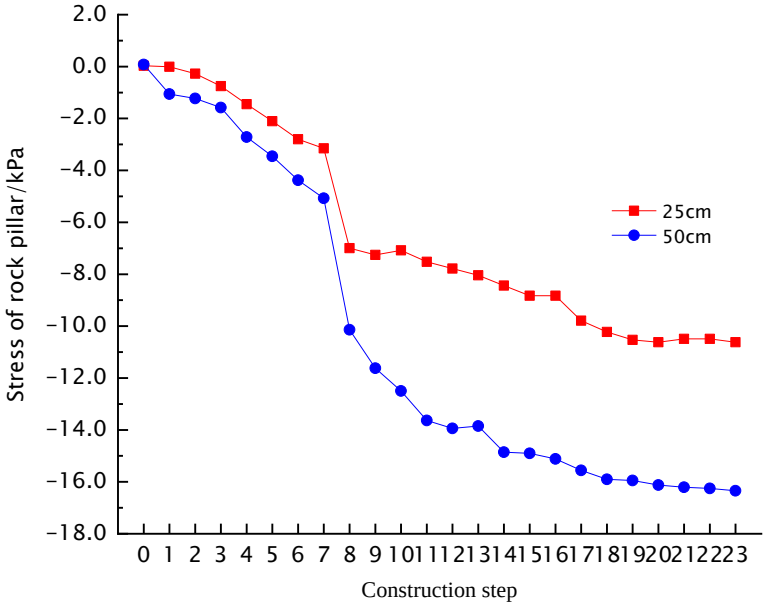

(**c**)

Figure 9. Stress variation curves of surrounding rock under different sidewall excavation widths and different construction steps at a rock wall slope of 80°. (**a**) Stress of the vault and sidewall near the mountain; (**b**) stress of tunnel floor and sidewall near the cliff; (**c**) stress of rock pillar.

As shown in Figure 9, the radial compressive stress of the vault gradually increased with the advancement of the excavation, with a maximum increase of 1.5 kPa. After excavation of step 7 in the monitoring section, the compressive stress decreased by 5.5 kPa due to load release and stabilization. The difference in stress changes under various conditions was small, indicating that the width of the opening on the sidewall had little effect on the radial compressive stress of the vault. The trend in radial compressive stress on the tunnel floor was similar to that in the vault, with a maximum increase of 8 kPa, and unloading during excavation reduced the compressive stress by 12 kPa. The radial compressive stress on both sidewalls significantly increased after excavation to the monitoring section. On the sidewall near the mountain, at w = 25 cm, the radial compressive stress increased by 2.25 kPa, and at w = 200 cm, it increased by 2.61 kPa, increasing by 16% compared to the former. On the sidewall near the cliff, at w = 25 cm, the radial compressive stress grew by 2.4 kPa, and at w = 50 cm, it increased by 2.63 kPa, i.e., by 9.6%. Due to the sidewall excavation, its stress could not be measured at w = 200 cm. The tunnel sidewall near the cliff was closer to the free surface, and its stress variation exceeded that of the sidewall near the mountain. The vertical compressive stress of the rock pillar was most affected by the width w of the sidewall opening. The compressive stress of the rock pillar at w = 25 cm increased by 10.6 kPa, while at w = 50 cm, it increased by 16.3 kPa, i.e., by 53.8% compared to the former. This indicates that the vertical compressive stress of the rock pillar was sensitive to the sidewall excavation width.

4.1.2. Tests with Varying Rock Wall Slopes

Stress analysis revealed the stress changes at each monitoring point during the excavation process compared with the initial state before excavation, as shown in Figure 10.

As shown in Figure 10, the tunnel vault was affected by excavation disturbance, and the radial stress increased as the excavation progressed. After excavation reached the monitoring section, the unloading stress dropped sharply, and the stress stabilized. This trend was consistent under slopes i of 80°, 85°, and 90°, with maximum changes of 5.8, 6.0, and 6.3 kPa, respectively; the latter two exceeding the former by 3.45% and 5%. The tunnel floor stress trend was consistent with that of the tunnel vault stress, but the change

was larger, with maximum changes of 12, 12.4, and 13 kPa, respectively; the latter two exceeding the former by 3.3% and 4.8%. The radial stress of the sidewall near the mountain decreased first and then increased as excavation progressed, with incremental changes of 2.25, 2.3, and 2.38 kPa under various working conditions, with increments of 2.2% and 3.4%. The stress increments of the tunnel sidewall near the cliff were 2.42, 2.52, and 2.67 kPa, with increments of 4.1% and 5.6%, with a larger change than the tunnel sidewall near the cliff due to the existence of side wall openings and free surfaces; the pressure on both sides of the tunnel is asymmetric. The rock pillar was the main load-bearing element of the open-side rock mass, with a relatively large vertical stress change compared to other monitoring points, with changes of 10.6, 11.1, and 11.7 kPa under the varying rock wall slopes, with increments of 4.7% and 5.4%. The stress variations at all positions were about 4%, indicating a slight effect of the rock wall slope variation on the tunnel's stress states.

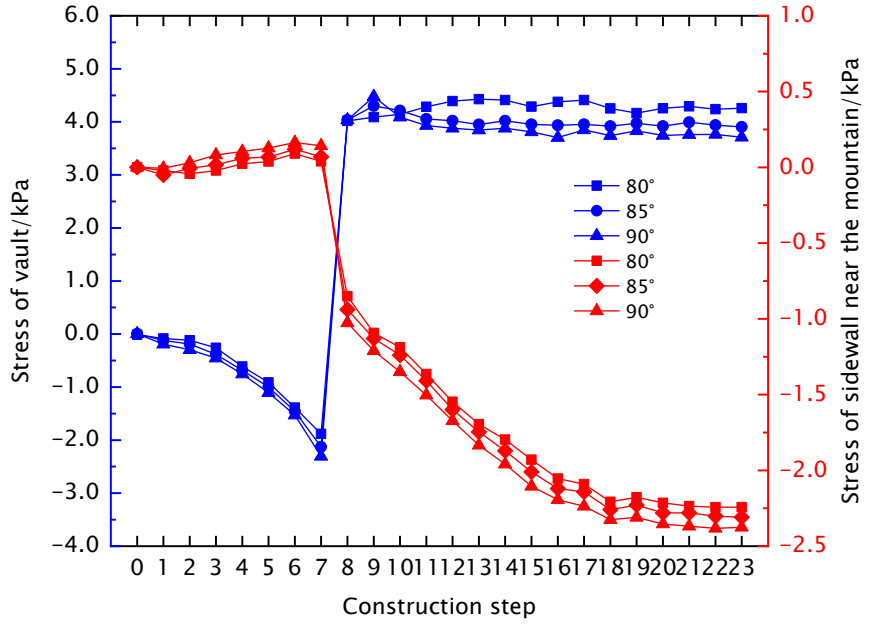

(**a**)

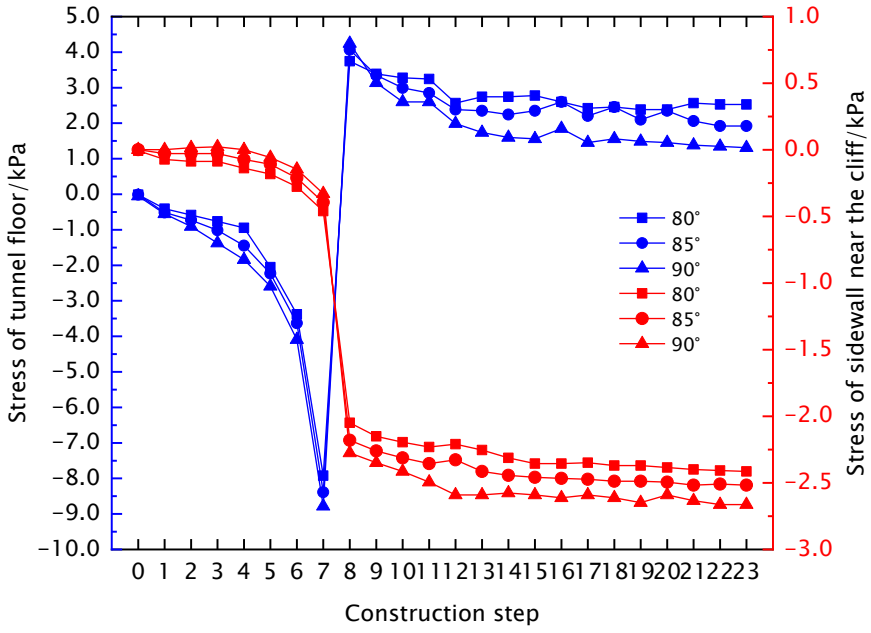

(**b**)

Figure 10. *Cont.*

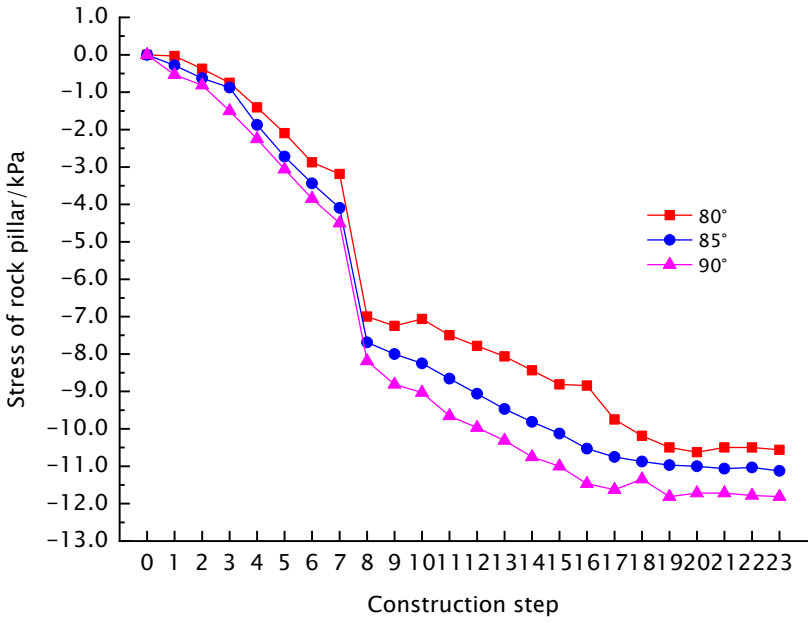

(**c**)

Figure 10. Stress variation curves of surrounding rock under rock wall slopes and different construction steps. (**a**) Stress of the vault and sidewall near the mountain; (**b**) stress of the tunnel floor and sidewall near the cliff; (**c**) stress of the rock pillar.

4.2. Surrounding Rock Displacement Distribution

4.2.1. Tests with Varying Sidewall Excavation Widths

During the excavation process of the tunnel, data collection was carried out through displacement meters embedded in the box body, monitoring the displacement evolution in the surrounding rock. Under different sidewall excavation widths w, the surrounding rock displacements were measured at four points, corresponding to the vault, the sidewall near the mountain, the sidewall opening top, and the hance near the mountain. Displacement probe elongation and contraction increased or decreased the initial micro-strain values, respectively. Therefore, positive values appear on the vault and sidewall opening tops, and negative values appear on the sidewalls and hances near the mountain. The radial displacement variation diagram of the surrounding rock under sidewall excavation widths is shown in Figure 11.

As shown in Figure 11, the displacement of each monitoring point positively correlated with the sidewall excavation width, and the variation was greater within a range of 1.5 times the diameter of the monitoring section. At the sidewall excavation widths w = 25 cm, 50 cm, and 200 cm, the displacements of the vault were 0.14, 0.17, and 0.21 mm, respectively; the latter two exceeding the former by 21.4% and 23.5%. The settlement of the sidewall opening top was larger than that of the vault, with displacements of 0.15, 0.2 and 0.25 mm, respectively, with increments of 33.3% and 31.6%. It can be seen that the sidewall excavation width had a greater impact on the displacement of the sidewall opening top. The displacement of the sidewall near the mountain was larger than that of the hance near the mountain, with displacement values of −0.053, −0.06 mm, and −0.072 mm, respectively, with the width of the sidewall opening with increments of 12.3% and 20.8%. The displacement values of the hance near the mountain were −0.045, −0.052, and −0.062 mm, respectively, with increments of 14.5% and 19.0%.

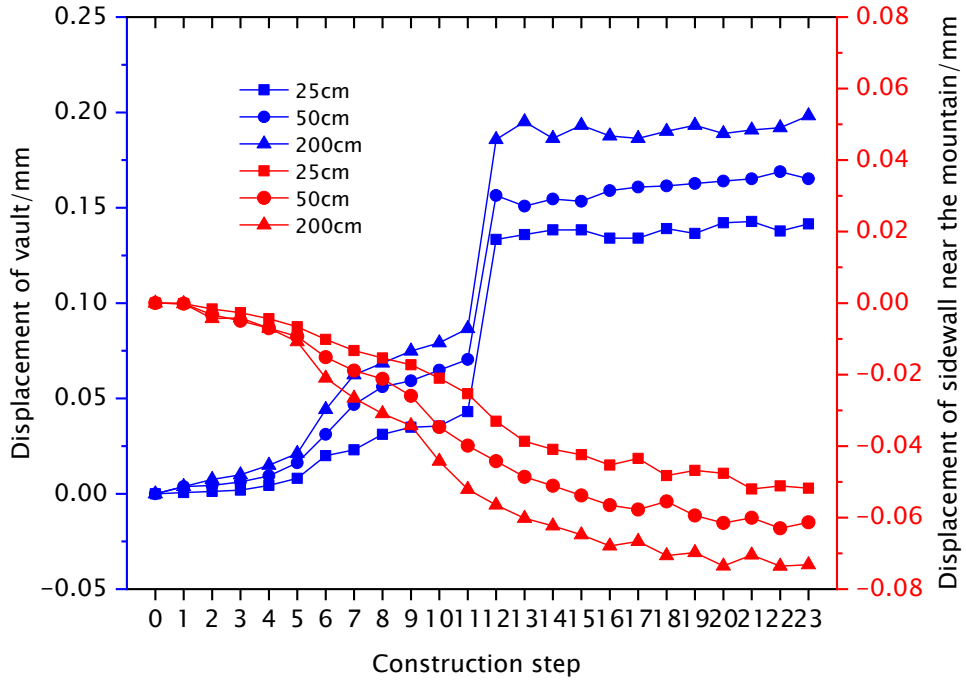

(**a**)

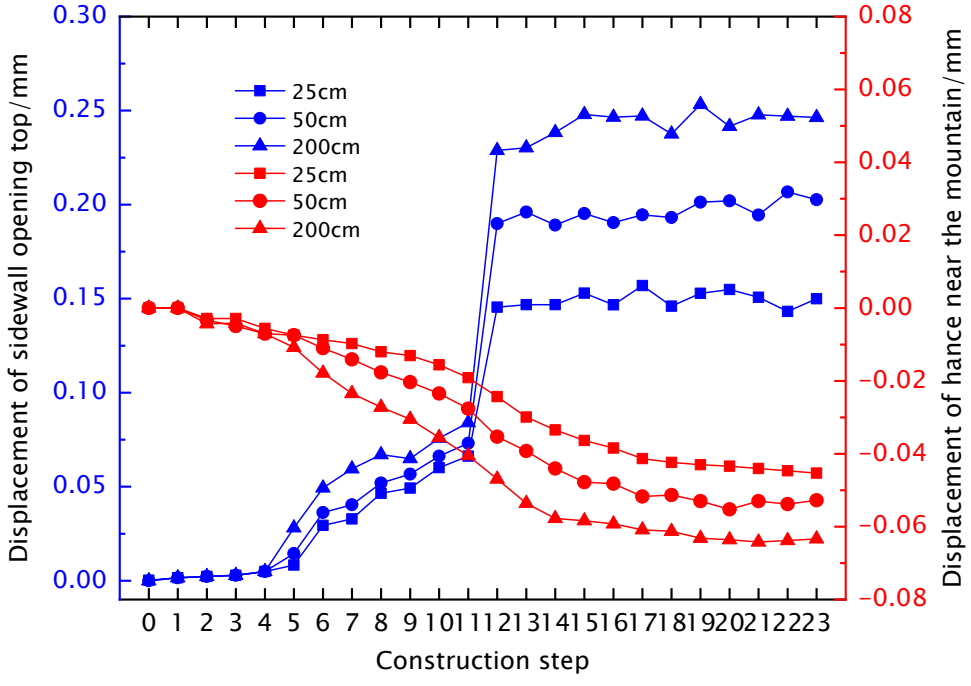

(**b**)

Figure 11. Radial displacement variation diagrams of the surrounding rock under sidewall excavation widths. (**a**) Displacement of the vault and sidewall near the mountain; (**b**) displacement of the sidewall opening top and hance near the mountain.

The displacement results can be ranked in decreasing order as follows: sidewall opening top > tunnel vault > sidewall near the mountain > hance near the mountain, due to the sidewall opening also forming a lateral "arch structure", similar to the deformation of the main tunnel; in addition, with its closer distance to the free face, the displacement of the sidewall opening top is more sensitive to the width of the sidewall opening compared to the tunnel.

4.2.2. Tests with Varying Rock Wall Slopes

The effect of different rock wall slopes on the displacement around the tunnel was studied to analyze the variation law, and collect the displacement changes in the vault, sidewall near the mountain, hance near the mountain, and sidewall opening top during excavation under three different rock wall slopes. The displacement curves of each measuring point during excavation are shown in Figure 12.

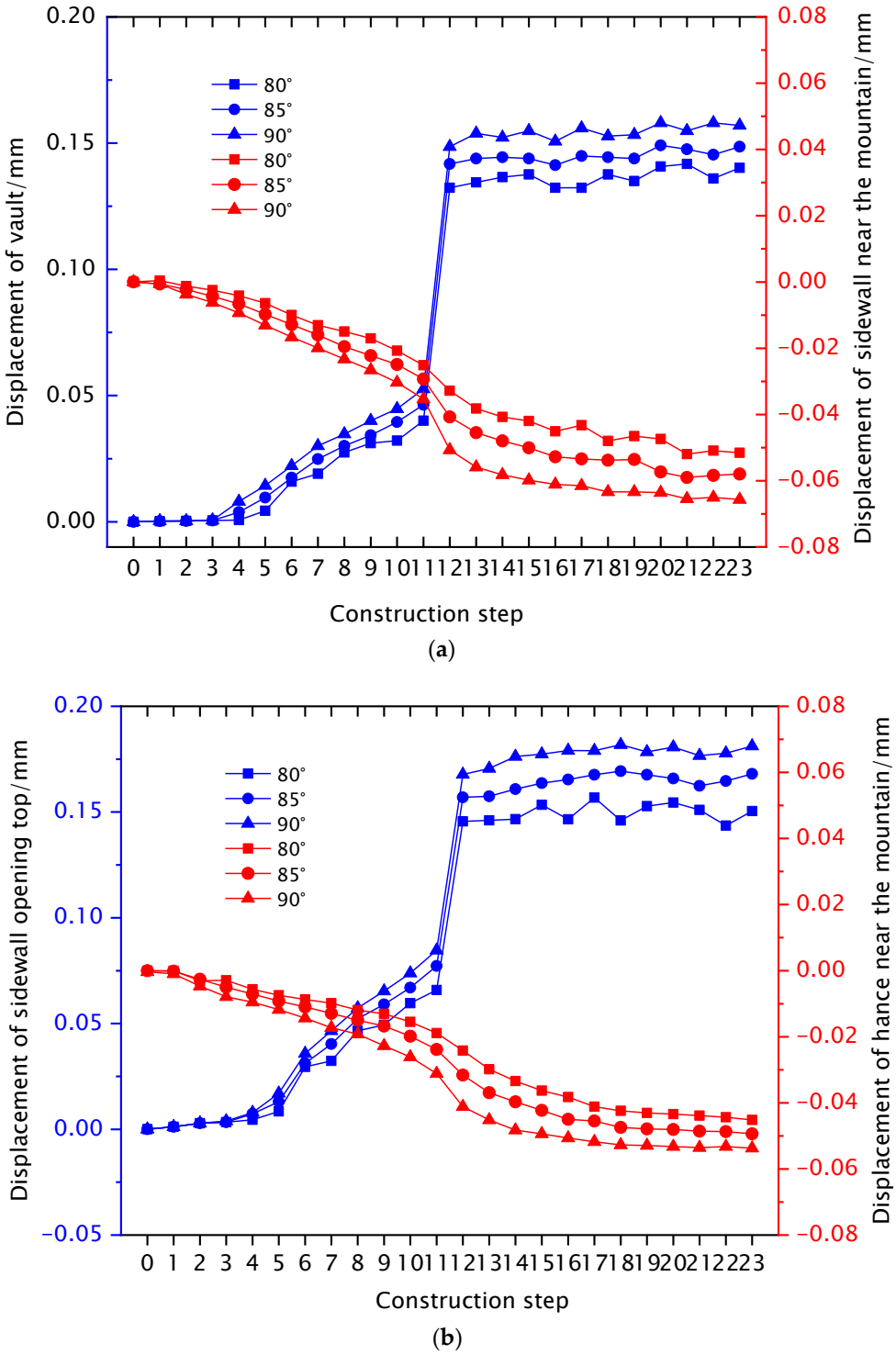

Figure 12. Radial displacement variation diagrams of the surrounding rock under different rock wall slopes. (**a**) Displacement of the vault and sidewall near the mountain; (**b**) displacement of the sidewall opening top and hance near the mountain.

As shown in Figure 12, the displacement of the tunnel vault changed significantly within 1.5 times the diameter of the monitoring section. At the rock wall slopes of i = 80°, 85°, and 90°, the displacements in the tunnel vault were 0.14, 0.15, and 0.16 mm, respectively, with increments of 7.1% and 6.7%. The displacement in the sidewall opening top was larger than that of the tunnel vault, reaching values of 0.152, 0.162, and 0.173 mm, with increments of 6.6% and 6.2%. Based on the relative displacement variations in the tunnel vault and sidewall opening top, it can be concluded that the change in rock wall slope had similar impacts on the two monitoring points. The radial displacement of the sidewall near the mountain increased continuously with excavation depth, with a steep increase in displacement when excavating in the monitored section, followed by a gradual decrease in the rate of change. The final displacements under each condition were −0.053, −0.058, and −0.066 mm, with increments of 9.4% and 12.1%. The displacement of the hance near the mountain was similar to that of the sidewall near the mountain, but with smaller changes in displacement, with values of −0.045, −0.049, and −0.054 mm, with increments of 8.8%, 10.2%. The rock wall slope effect on the displacement of the sidewall near the mountain was quite strong.

5. Discussions

5.1. Analysis of Surrounding Rock Displacement Law

The above PAM tests revealed that displacements of the sidewall opening top and the sidewall near the mountain were mainly affected by the sidewall excavation width and rock wall slope, respectively. To explore the law of surrounding rock displacement evolution with changes in sidewall excavation width and rock wall slope, the displacement values of the vaults and sidewall opening tops at w = 25~200 cm and those of the sidewall near the mountain at i = 80~90° were experimentally determined and converted to the prototype, according to the geometric similarity ratio of 1:20, as shown in Table 7. Due to the opening on the sidewall, the displacement data of the sidewall near the cliff could not be measured.

Table 7. Sidewall excavation width, rock wall slope, and surrounding rock displacement.

Sidewall Excavation Width/m	**5**	**10**	**40**
Displacement of sidewall opening top/mm	3.01	4.01	4.94
Displacement of vault/mm	2.83	3.31	3.97
Rock wall slope/°	**80**	**85**	**90**
Displacement of sidewall near the mountain/mm	1.06	1.16	1.32

From Table 7, it can be seen that the displacement of the tunnel vault and sidewall opening top increased with the sidewall excavation width, and that of the sidewall near the mountain increased with the rock wall slope, both exhibiting positive correlation. To quantitatively analyze the relationship between them, considering that the experiment with w = 40 m contained no sidewall, the opening width in the first few working conditions was that of a single opening. When the opening width in the sidewall condition was adjusted to w = 13.3 m for fitting, the displacement curves were constructed for the sidewall opening top under different sidewall excavation widths and for the sidewall near the mountain under different rock wall slopes, as shown in Figure 13. From Figure 13, it can be seen that the width of the sidewall opening was practically exponential with the vault displacement value, the latter sharply increasing with the former growth. The width of the sidewall opening were nearly linearly distributed with the sidewall opening top and sidewall near the mountain displacement value, the latter increasing with the former growth.

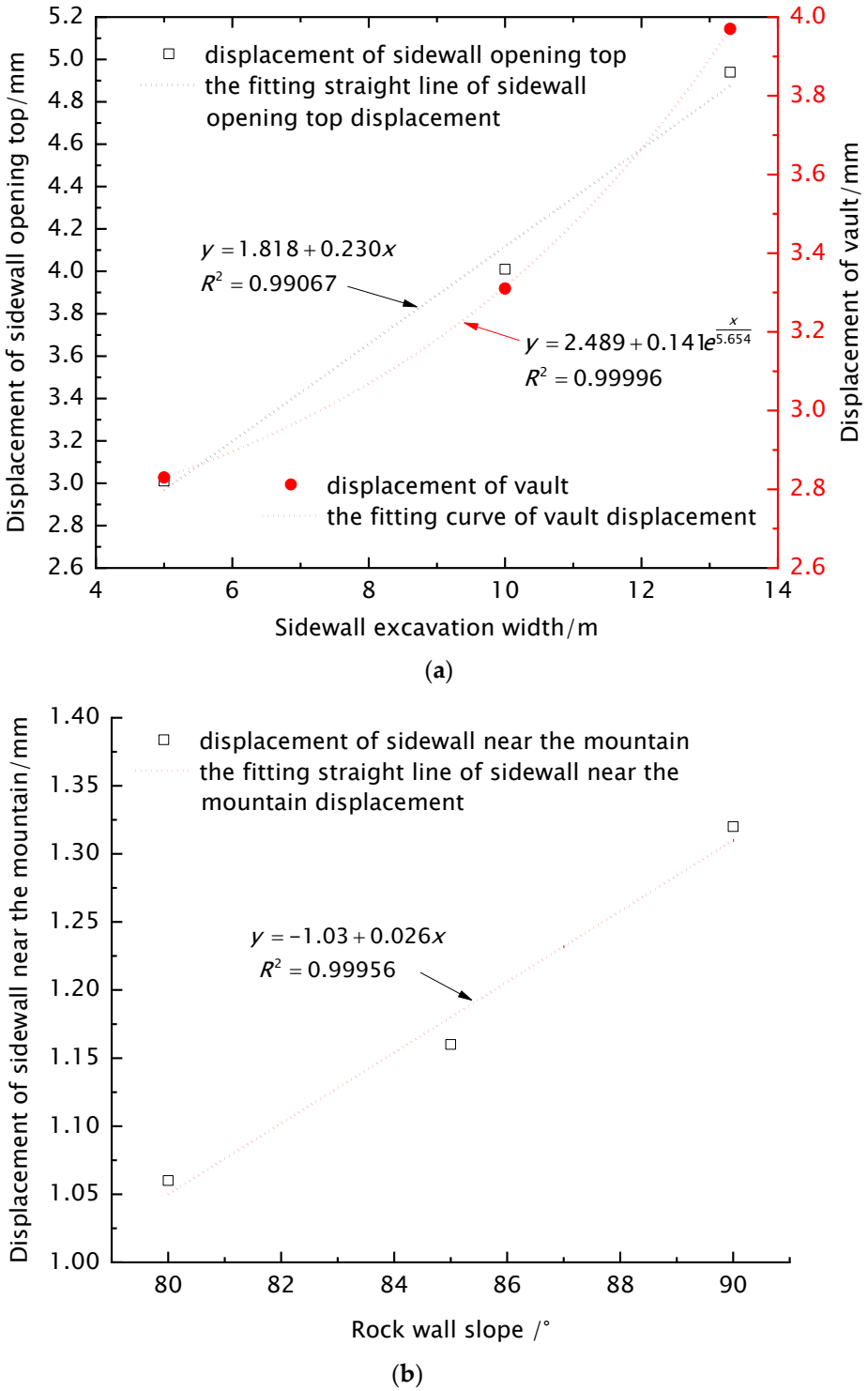

Figure 13. Relationship between surrounding rock displacement and sidewall excavation width, and rock wall slope. (**a**) Relationship diagram between the displacement of sidewall opening top, vault and the sidewall excavation width; (**b**) relationship diagram between the displacement of sidewall near mountain and rock wall slope.

5.2. Comparison of Numerical Simulation and PAM Test Results

Using the finite difference software FLAC3D 6.0 for numerical simulation calculations, the Drucker–Prager model was adopted as the constitutive model, with the physical and mechanical parameters of the surrounding rock listed in Table 5. The coordinate system

implied the X-axis perpendicular to the tunnel axis, with the direction to the right as positive; the Y-axis was parallel to the tunnel axis, with the direction inward as positive; and the Z-axis coincided with the vertical direction, with upward as positive. The boundary range was as follows: in the X direction, four times the diameter of the tunnel was taken to the right from the tunnel boundary, and the left, the tunnel was taken to the rock wall with a clearance face of 3 m, which was the sidewall thickness based on the supporting engineering; in the Y direction, four times the diameter of the tunnel was taken. In the Z direction, from the upper boundary of the tunnel to the ground surface, the burial depth was 31 m, and the lower boundary was taken as four times the diameter of the tunnel, with an overall model size of 47 m (X-direction) × 35.2 m (Y-direction) × 72.75 m (Z-direction). The surrounding rock was simulated using hexahedral solid elements, with a total of 182,351 nodes and 176,710 elements in the model. Z-direction displacement constraints were applied to the bottom of the model, X-axis positive direction displacement constraints were applied to the right side of the model, Y-direction displacement constraints were applied to the front and back sides of the model, and the top surface and X-axis negative direction were free surfaces. The model was subdivided into grids before and after excavation, as shown in Figure 14.

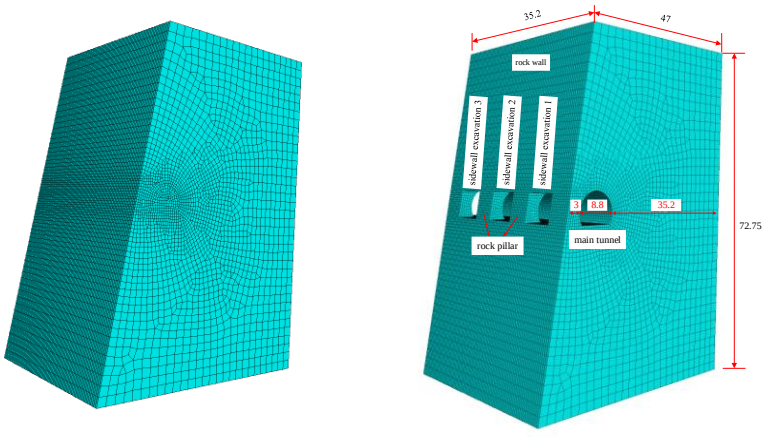

(**a**) (**b**)

Figure 14. Overall and grid map after excavation (unit: m). (**a**) The configuration of the numerical model before excavation; (**b**) the configuration of the numerical model after excavation.

A numerical simulation of hanging tunnel excavation was performed via FLAC3D 6.0, computing displacement and stress variations in the surrounding rocks for different sidewall excavation widths and rock wall slopes. When performing numerical simulation, no external load was applied and only the weight of the surrounding rock itself was considered. The numerical results were compared with the PAM test results. The displacement of the middle section of the hance near the mountain, the tunnel vault, and the sidewall opening top with a rock wall slope $i = 80°$ and a sidewall excavation width of 500 cm were selected for comparative analysis, as shown in Figure 15.

As can be seen in Figure 15, when the PAM results were converted to the prototype according to the similarity coefficients, the PAM-derived displacements in the hance near the mountain, vault, and sidewall opening top near the mountain generally exceeded the respective numerical results. It can be seen that the final displacement convergence value of the PAM is approximately twice that of the numerical simulation method. But both methods showed a sudden displacement change during excavation steps 11 to 12, and the trend in the change was consistent, indicating that the disturbance patterns during the excavation process were consistent for both methods. The observed discrepancies between numerical and PAM test results can be attributed to simplified boundary conditions, selection of analog material parameters, similarity coefficients and excavation simulation. Since PAM

test and numerical curves exhibited the same trend, the numerical verification proved the proposed PAM model efficiency.

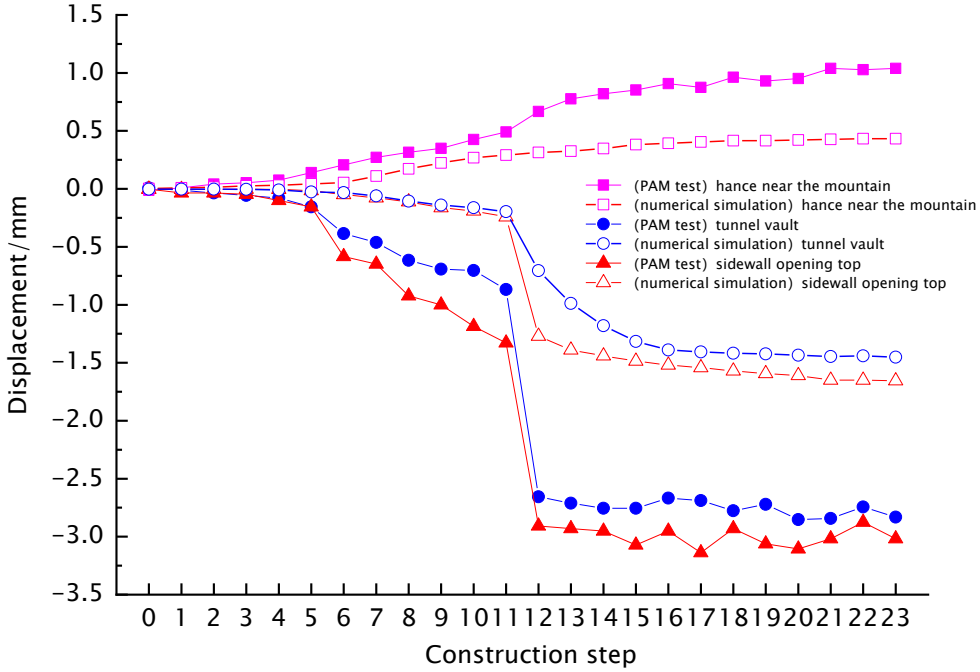

Figure 15. Comparison of displacements obtained by numerical simulation and PAM tests.

When conducting numerical simulation calculations, they are based on the actual parameters of the engineering prototype. In PAM experiments, the selection of similar materials cannot be completely consistent with the prototype, coupled with the influence of factors such as tunnel model construction and excavation process simulation, resulting in certain differences in displacement values between the two methods. However, their changing trends are consistent, achieving the purpose of mutual verification. Therefore, numerical simulation model can be used to predict and analyze the behavior of the hanging tunnels.

6. Conclusions

The stress and displacement variations during the excavation of the hanging tunnel with three different rock wall slopes (80°, 85°, 90°) and three sidewall excavation widths (25, 50, and 200 cm) were studied by conducting physical analog model (PAM) tests. The variation patterns were analyzed, and the following conclusions were drawn:

(1) The radial stress of the vault and floor of the tunnel increased gradually as the excavation face advanced. After excavation to the monitored section, the stress dropped sharply due to unloading. The radial stress on the two sidewalls changed inconsistently, and the vertical stress in the rock pillar gradually grew during the excavation process. The maximum increment in the vertical stress of the rock pillar due to the sidewall excavation width variation was 53.8%, exceeding those of other positions in the hanging tunnel; the rock wall slope variation changed stresses of the monitoring points around the tunnel only by 4%, indicating its slight effect on the hanging tunnel stressed state.

(2) The hanging tunnel excavation caused the vault to sink, the tunnel floor to rise, and the sidewall opening top to sink. Due to the lack of support near the rock wall, the sidewall and the hance near the mountain deformed toward the mountain side. The sidewall opening top displacement positively correlated with the sidewall excavation width and the rock wall slope. The former parameter had a stronger effect on the

sidewall opening top displacement, while the latter on the sidewall displacement, providing a certain reference for similar engineering projects.

(3) The surrounding rock displacement and stress variation trends obtained via PAM tests were numerically verified, yielding similar curves for various sidewall excavation widths and rock wall slopes, proving the proposed model feasibility.

(4) Although there is no on-site measurement data in this article, two methods, PAM experiments and numerical simulation, were used for mutual verification, and the results are reliable. In the future, if conditions are suitable, on-site monitoring of actual projects can be carried out to further verify the reliability of the tests.

(5) This article assumes that the surrounding rock of the tunnel is a homogeneous body, but in actual engineering, the surrounding rock is a non-homogeneous body with groundwater present, as well as faults and joints. In the future, we will conduct analysis and research on the impact of faults, joints, and other factors on the stability of tunnel-surrounding rock.

Author Contributions: Conceptualization, Z.C., T.W. and Z.X.; methodology, Z.C., H.Z. and T.W.; software, Z.C., Z.X. and D.Z.; validation, H.Z., Z.C. and T.W.; formal analysis, H.Z. and Z.C.; investigation, Z.C., T.W. and D.Z.; resources, Z.C., H.Z. and T.L.; data curation, Z.X., D.Z., B.L. and H.F.; writing—original draft preparation, T.W., Z.C., Z.X. and D.Z.; writing—review and editing, T.W. and Z.C.; visualization, T.W., Z.C. and H.F.; supervision, Z.C., T.W. and T.L.; project administration, Z.C., T.L. and B.L.; funding acquisition, H.Z. and Z.C. All authors have read and agreed to the published version of the manuscript.

Funding: This research was funded by the Scientific and Technological Research Program of Chongqing Municipal Education Commission (Grant No. KJQN202005703) and the Natural Science Foundation of Chongqing (Grant No. cstc2021jcyj-msxmX1048).

Data Availability Statement: The original contributions presented in the study are included in the article, further inquiries can be directed to the corresponding authors.

Acknowledgments: We extend our sincere gratitude to Xianpu Han of Bijie Daily in Guizhou Province for his invaluable contribution to this research by providing onsite photographs of the Shibanhe hanging tunnel.

Conflicts of Interest: Authors Hao Zhang, Zhao Xiang and Zhiwei Cai were employed by the company CCTEG Chongqing Engineering (GROUP) Co., Ltd. Author Dong Zhang was employed by the company Qinyuan Technology Co., Ltd. Author Hu Feng was employed by the company Chongqing Mas Sci. & Tech. Co., Ltd. The remaining authors declare that the research was conducted in the absence of any commercial or financial relationships that could be construed as a potential conflict of interest.

References

1. Available online: https://www.gov.cn/lianbo/bumen/202306/content_6887539.htm (accessed on 10 August 2024).
2. Anbalagan, R.; Singh, B.; Bhargava, P. Half tunnels along hill roads of Himalaya—An innovative approach. *Tunn. Undergr. Space Technol.* **2003**, *18*, 411–419. [CrossRef]
3. Emad, M.; Khan, M.; Raza, M.; Saki, S.; Aijaz, M.; Tahir, M. Optimum design of half tunnels for transportation in the Himalayas. *Transp. Infrastruct. Geotechnol.* **2022**, *9*, 101–116. [CrossRef]
4. Available online: https://h.xinhuaxmt.com/vh512/share/6244427?d=13415a0&channel (accessed on 10 August 2024).
5. Available online: https://h.xinhuaxmt.com/vh512/share/9650463?d=1343f0c&channel (accessed on 10 August 2024).
6. Available online: https://www.chinadaily.com.cn/a/202110/22/WS61721009a310cdd39bc707b2.html (accessed on 10 August 2024).
7. Hoek, E.; Brown, E.T. *Underground Excavations in Rock*; Institution of Mining and Metallurgy: London, UK, 1980.
8. Carranza-Torres, C.; Fairhurst, C. Application of the Convergence-Confinement method of tunnel design to rock masses that satisfy the Hoek-Brown failure criterion. *Tunn. Undergr. Space Technol.* **2000**, *15*, 187–213. [CrossRef]
9. Deere Don, U.; Deere Don, W. Rock quality designation (RQD) after twenty years. In *U.S. Army Corps of Engineers Contract Report GL-89-1*; Waterways Experiment Station: Vicksburg, MI, USA, 1989.
10. Hoek, E.; Diederichs, M.S. Empirical estimation of rock mass modulus. *Int. J. Rock Mech. Min.* **2006**, *43*, 203–215. [CrossRef]
11. Cai, M.F.; Kaiser, P.K.; Tasaka, Y.; Minami, M. Determination of residual strength parameters of jointed rock masses using the GSI system. *Int. J. Rock Mech. Min.* **2007**, *44*, 247–265. [CrossRef]

12. Singh, B.; Goel, R.K.; Jethwa, J.L.; Dube, A.K. Support pressure assessment in arched underground openings through poor rock masses. *Eng. Geol.* **1997**, *48*, 59–81. [CrossRef]
13. Terzaghi, K. *Theoretical Soil Mechanics*; Wiley and Sons: Hoboken, NJ, USA, 1943; pp. 195–202.
14. Barton, N.; Lien, R.; Lunde, J. Engineering classification of rock masses for the design of tunnel support. *Rock Mesh.* **1974**, *6*, 189–236. [CrossRef]
15. *JTG 3370.1-2018*; Specifications for Design of Highway Tunnels Section 1 Civil Engineering. China Merchants Chongqing Communications Technology Research and Design Institute Co., Ltd.: Beijing, China; China Communications Press: Beijing, China, 2018.
16. Fraldi, M.; Guarracino, F. Limit analysis of progressive tunnel failure of tunnels in Hoek-Brown rock masses. *Int. J. Rock Mech. Min.* **2012**, *50*, 170–173. [CrossRef]
17. Cai, W.Q.; Zhu, H.H.; Liang, W.H. Three-dimensional tunnel face extrusion and reinforcement effects of underground excavations in deep rock masses. *Int. J. Rock Mech. Min.* **2022**, *150*, 104999. [CrossRef]
18. Perazzelli, P.; Leone, T.; Anagnostou, G. Tunnel face stability under seepage flow conditions. *Tunn. Undergr. Space Technol.* **2014**, *43*, 459–469. [CrossRef]
19. Liang, Q.; Xu, J.J.; Wei, Y.G. Three-dimensional stability analysis of tunnel face based on unified strength theory. *Sci. Rep.* **2023**, *13*, 12326. [CrossRef] [PubMed]
20. Ukritchon, B.; Keawsawasvong, S. Stability of unlined square tunnels in Hoek-Brown rock masses based on lower bound analysis. *Comput. Geotech.* **2019**, *105*, 249–264. [CrossRef]
21. Wang, Y.C.; Jing, H.W.; Su, H.J.; Xie, J.Y. Effect of a fault fracture zone on the stability of tunnel-surrounding rock. *Int. J. Geomech.* **2017**, *17*, 837. [CrossRef]
22. Zhang, Z.Q.; Chen, F.F.; Li, N.; Swoboda, G.; Liu, N.F. Influence of fault on the surrounding rock stability of a tunnel: Location and thickness. *Tunn. Undergr. Space Technol.* **2017**, *61*, 1–11. [CrossRef]
23. Ding, Z.D.; Ji, X.F.; Li, X.Q.; Ren, Z.H.; Zhang, S. Influence of symmetric and asymmetric voids on mechanical behaviors of tunnel linings: Model tests and numerical simulations. *Symmetry* **2019**, *11*, 802. [CrossRef]
24. Zheng, H.B.; Li, P.F.; Ma, G.W. Stability analysis of the middle soil pillar for asymmetric parallel tunnels by using model testing and numerical simulations. *Tunn. Undergr. Space Technol.* **2020**, *108*, 103686. [CrossRef]
25. Jiang, Q.; Song, S.G.; Li, T.; Wang, K.; Gu, R.H. Study on surrounding rock stability of small clear-distance twin highway tunnel with eight lanes. *Geotech. Geol. Eng.* **2019**, *37*, 593–598. [CrossRef]
26. Zhen, C.; Li, J.H.; Fu, X.W.; Sheng, Q.; Zhou, G.X.; Ma, Y.L.N.; Wang, T.Q. Evaluating the response of a tunnel subjected to strike-slip fault rupture in conjunction with model test and hybrid discrete-continuous numerical modeling. *Rock Mech. Rock Eng.* **2022**, *55*, 4743–4764. [CrossRef]
27. He, P.; Li, S.C.; Li, L.P.; Zhang, Q.Q.; Xu, F.; Chen, Y.J. Discontinuous deformation analysis of super section tunnel surrounding rock stability based on joint distribution simulation. *Comput. Geotech.* **2017**, *91*, 218–229. [CrossRef]
28. Xiang, Y.Z.; Zeng, Z.K.; Xiang, Y.J.; Abi, E.D.; Zheng, Y.R.; Yuan, H.C. Tunnel failure mechanism during loading and unloading processes through physical model testing and DEM simulation. *Sci. Rep.* **2021**, *11*, 16753. [CrossRef]
29. Li, C.C.; Mo, Z.G.; Jiang, H.B.; Yang, F.C. Analysis of the stability and mechanical characteristics of the jointed surrounding rock and lining structure of a deeply buried hydraulic tunnel. *Fluid Dyn. Mater. Proc.* **2022**, *18*, 29–39. [CrossRef]
30. Chen, H.M.; Yu, H.S.; Smith, M.J. Physical model tests and numerical simulation for assessing the stability of brick-lined tunnels. *Tunn. Undergr. Space Technol.* **2016**, *53*, 109–119. [CrossRef]
31. Vazaios, I.; Diederichs, M.S.; Vlachopoulos, N. Assessment of strain bursting in deep tunnelling by using the finite-discrete element method. *J. Rock Mech. Geotech. Eng.* **2018**, *11*, 12–37. [CrossRef]
32. Fu, H.L.; Deng, H.S.; Zhao, Y.B.; Chang, X.B.; Yi, H.D. Study on the disturbance of existing subway tunnels by foundation sloping excavation. *Appl. Sci.* **2023**, *13*, 948. [CrossRef]
33. Wang, L.X.; Zhu, Z.D.; Zhu, S.; Wu, J.Y. A case study on tunnel excavation stability of columnar jointed rock masses with different dip angles in the Baihetan diversion tunnel. *Symmetry* **2023**, *15*, 1232. [CrossRef]
34. Ma, H.P.; Daud, N.N.N.; Yusof, Z.M.; Yaacob, W.Z.; He, H.J. Stability analysis of surrounding rock of an underground cavern group and excavation scheme optimization: Based on an optimized DDARF method. *Appl. Sci.* **2023**, *13*, 2152. [CrossRef]
35. Panji, M.; Koohsari, H.; Adampira, M.; Alielahi, H.; Asgari Marnani, J. Stability analysis of shallow tunnels subjected to eccentric loads by a boundary element method. *J. Rock Mech. Geotech. Eng.* **2016**, *8*, 480–488. [CrossRef]
36. Schlotfeldt, P.; Elmo, D.; Panton, B. Overhanging rock slope by design: An integrated approach using rock mass strength characterisation, large-scale numerical modelling and limit equilibrium methods. *J. Rock Mech. Geotech. Eng.* **2018**, *10*, 72–90. [CrossRef]
37. Tokashiki, N.; Aydan, Ö. The stability assessment of overhanging Ryuku limestone cliffs with an emphasis on the evaluation of tensile strength of rock mass. *Doboku Gakkai Ronbunshuu C* **2010**, *66*, 397–406. [CrossRef]
38. Yuan, B.X.; Liang, J.K.; Lin, H.Z.; Wang, W.Y.; Xiao, Y. Experimental Study on Influencing Factors Associated with a New Tunnel Waterproofing for Improved Impermeability. *J. Test. Eval.* **2024**, *52*, 344–363.
39. Fang, Q.A.; Zhang, D.L.; Li, Q.Q.; Wong, L.N.Y. Effects of twin tunnels construction beneath existing shield-driven twin tunnels. *Tunn. Undergr. Space Technol.* **2015**, *45*, 128–137. [CrossRef]

40. Xue, Y.D.; Zhao, F.; Zhao, H.X.; Li, X.; Diao, Z.X. A new method for selecting hard rock TBM tunnelling parameters using optimum energy: A case study. *Tunn. Undergr. Space Technol.* **2018**, *78*, 64–75. [CrossRef]
41. Tian, Q.Y.; Zhang, J.T.; Zhang, Y.L. Similar simulation experiment of expressway tunnel in karst area. *Constr. Build. Mater.* **2018**, *176*, 1–13. [CrossRef]
42. Huang, F.; Zhu, H.H.; Xu, Q.W.; Cai, Y.C.; Zhuang, X.Y. The effect of weak interlayer on the failure pattern of rock mass around tunnel–Scaled model tests and numerical analysis. *Tunn. Undergr. Space Technol.* **2013**, *35*, 207–218. [CrossRef]
43. Wu, J.; Fu, H.; Zhang, L.W.; Zhang, X.Y.; Guo, D.Y. Stability analysis of surrounding rock in underground chamber excavation of coral reef limestone. *Rock Mech. Rock Eng.* **2022**, *55*, 4717–4742. [CrossRef]
44. Xu, Z.L.; Luo, Y.B.; Chen, J.X.; Su, Z.M.; Zhu, T.T.; Yuan, J.P. Mechanical properties and reasonable proportioning of similar materials in physical model test of tunnel lining cracking. *Constr. Build. Mater.* **2021**, *300*, 123960. [CrossRef]
45. Zhao, W.S.; Gao, H.; Chen, W.Z.; Liu, J.G.; Peng, W.B.; Zhou, S. Experimental study on similar materials for tunnel lining concrete in geomechanical model tests. *Eng. Fail. Anal.* **2023**, *152*, 107456. [CrossRef]
46. Jiang, N.; Guo, P.P.; Zhang, H.; Lu, F.Q.; Liu, J. Mechanical behavior of a new similar material for weathered limestone in karst area: An experimental investigation. *Appl. Rheol.* **2023**, *33*, 20220154. [CrossRef]
47. Lei, M.F.; Peng, L.M.; Shi, C.H. Model test to investigate the failure mechanisms and lining stress characteristics of shallow buried tunnels under unsymmetrical loading. *Tunn. Undergr. Space Technol.* **2015**, *46*, 64–75. [CrossRef]
48. Lin, P.; Liu, H.Y.; Zhou, W.Y. Experimental study on failure behaviour of deep tunnels under high in-situ stresses. *Tunn. Undergr. Space Technol.* **2015**, *46*, 28–45. [CrossRef]
49. Xu, S.S.; Lei, H.; Li, C.; Liu, H.Q.; Lai, J.X.; Liu, T. Model test on mechanical characteristics of shallow tunnel excavation failure in gully topography. *Eng. Fail. Anal.* **2021**, *119*, 104978. [CrossRef]
50. Peng, L.F.; Hu, X.C.; Su, G.S.; Qin, Z.H.; Lu, H.; He, B.Y. Cracking characteristics of the surrounding rocks of a hydraulic tunnel under high geothermal conditions: A model test. *Rock Mech. Rock Eng.* **2021**, *54*, 1369–1390. [CrossRef]